Exact solution of the single impurity problem in nonreciprocal lattices: Impurity-induced size-dependent non-Hermitian skin effect

Yanxia Liu,[1] Yumeng Zeng,[1,2] Linhu Li,[3,*] and Shu Chen[1,2,4,†]

[1]*Beijing National Laboratory for Condensed Matter Physics, Institute of Physics, Chinese Academy of Sciences, Beijing 100190, China*

[2]*School of Physical Sciences, University of Chinese Academy of Sciences, Beijing 100049, China*

[3]*Guangdong Provincial Key Laboratory of Quantum Metrology and Sensing & School of Physics and Astronomy, Sun Yat-Sen University (Zhuhai Campus), Zhuhai 519082, China*

[4]*Yangtze River Delta Physics Research Center, Liyang, Jiangsu 213300, China*

(Received 7 June 2021; revised 14 July 2021; accepted 20 July 2021; published 2 August 2021)

Non-Hermitian nonreciprocal systems are known to be extremely sensitive to boundary conditions, exhibiting diverse localizing behaviors and spectrum structures when translational invariance is locally broken, either by tuning the boundary coupling strength, or by introducing an effective boundary using impurities or defects. In this work we consider the single impurity problem in the Hatano-Nelson model and the Su-Schreieffer-Heeger model, which can be exactly solved with the single impurity being treated as an effective boundary of the system. From our exact solutions for finite-size systems, we unveil that increasing the impurity strength can lead to a transition of the bulk states from nonskin states to skin states, accompanied by the change of the spectrum structure from an ellipse in the complex plane to a segment along the real axis. These exact results indicate that the critical value of impurity strength is size dependent, and increases exponentially with the lattice size when the impurity is strong or the system is large enough. Our exact solutions are also useful for determining the spectral topological transition in the concerned models.

DOI: 10.1103/PhysRevB.104.085401

I. INTRODUCTION

Boundary conditions play a pivotal role in determining the properties of a wide variety of physical systems, ranging from the most fundamental problem of solving a single-particle Schrödinger equation, to more stimulating emergent phenomena such as the quantum Hall effect, where the quantized Hall conductance is associated with the number of topological states localized at the physical boundaries of the system. In contrast, the bulk energy spectra are usually expected to be insensitive to boundary perturbations, as their corresponding eigenstates are mostly distributed in the bulk of the system. However, this picture generally fails when non-Hermiticity is introduced to the Hamiltonian, where the spectra under periodic and open boundary conditions (PBC and OBC) can dramatically diverge from each other [1]. Physically, such a significant boundary effect can be understood with the non-Hermitian skin effect (NHSE), namely a majority of eigenstates are pumped to the boundaries by the nonreciprocity of the system under OBC [2]. To date, the NHSE has been extensively investigated in various systems [2–34], as it is known to be associated with many intriguing non-Hermitian phenomena, e.g., the breakdown of conventional bulk boundary correspondence [2,35], the spectral point-gap topology [28–30], the critical NHSE [31,32], and the directional signal amplification [33,34].

Beyond the PBC and OBC, much effort has been made recently in exploring non-Hermitian systems with other types of boundary conditions. It has been found that by tuning the strength of boundary hoppings away from both the PBC and OBC, a new type of so-called scale-free accumulating states emerges in a finite-size system, and the NHSE becomes less stable against such boundary perturbations when increasing the system's size [36,37]. The continuous deformation between the PBC and OBC also provides more insight of the NHSE [9,38], and leads to a topological quantized response unique in non-Hermitian systems [39]. On the other hand, strong impurities and defects effectively induce a boundary in a periodic system, and may act as the OBC for boundary phenomena in either Hermitian and non-Hermitian systems [40–46]. Besides crossover from PBC to OBC, in two- or three-dimensional non-Hermitian systems, introducing dislocations effectively gives a new type of boundary conditions, which can induce the NHSE and exhibit interesting topological effects [47–49].

In this paper we analytically study the single impurity problem in two representative one-dimensional (1D) non-Hermitian models that exhibit the NHSE under OBC, namely the Hatano-Nelson (HN) model and the nonreciprocal Su-Schreieffer-Heeger (SSH) model. In both cases, exact solutions are obtained with a single on-site impurity potential, whose strength varies from zero to infinity. The bulk states are seen to go through a transition from nonskin states to skin states at certain critical values of the impurity strength, after which their eigenenergies become purely real. In other words, a strong impurity behaves similarly as the OBC, except for the

*lilh56@mail.sysu.edu.cn
†schen@iphy.ac.cn

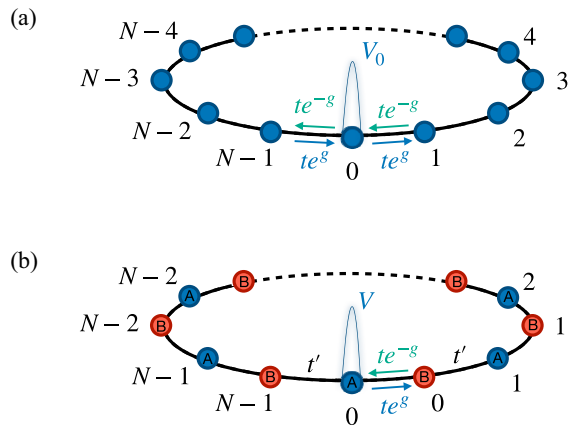

FIG. 1. (a) The Hatano-Nelson model with one impurity. (b) The nonreciprocal SSH model with one impurity.

bound state localized at the impurity. The transition value of the impurity strength is found to depend on the system's size and the nonreciprocity strength of the system, and also varies for different eigenstates. We have also applied our results to study the spectral topology of these two models, and the topological transition points are accurately predicted by our exact solutions.

The rest of the paper is organized as follows. In Sec. II we present the exact solutions for the single-impurity problem in the HN model, and analyze in details the transition for the bulk states from nonskin to skin states. In Sec. III we study the single-impurity problem for the nonreciprocal SSH model, where exact solutions can be obtained by mapping it to the HN model. We then apply our exact solutions to identify the topological transition points of the spectral topology of the two models in Sec. IV. Finally, a summary of our results is given in Sec. V.

II. SINGLE IMPURITY PROBLEM FOR ONE-BAND 1D NONRECIPROCAL LATTICE

We consider a 1D HN chain [50] with an impurity under the periodic boundary condition [see Fig. 1(a)]. The HN chain is originally proposed for investigating localization of the bound states induced by a disorder, provided its strength is compatible to that of the nonreciprocity of the system. In our model, however, there can be only a single bound state at the impurity, and in the following discussion we are mainly focusing on a different localization mechanism, namely the skin localization induced by the nonreciprocity. The Hamiltonian is given by

$$H_{\mathrm{NH}} = \sum_{n=0}^{N-1} (t_L|n\rangle\langle n+1| + t_R|n+1\rangle\langle n|) + V_0|0\rangle\langle 0|, \quad (1)$$

where $t_{R(L)}$ denotes the right (left)-hopping amplitude which can be parametrized as $t_L = te^{-g}$ and $t_R = te^{g}$ with real t and g. Here we set $t = 1$ as the energy unit. The asymmetry of hopping amplitudes ($g \neq 0$) leads to the non-Hermiticity of the model. Nevertheless, the Hamiltonian is pseudo-Hermitian as it satisfies $H^\dagger = PHP$ with P the parity operator. That is, the Hamiltonian H becomes $H^\dagger$ when exchanging sites i and $N-i$ in Fig. 1(a). Therefore the eigenenergies of H are either real, or given by complex conjugated pairs.

The Schrödinger equation $H|\psi\rangle = \epsilon|\psi\rangle$ with the wave function $|\psi\rangle = \sum_n \psi_n|n\rangle$ can be written as a second order homogeneous linear difference equation

$$e^{g}\psi_{n-1} + e^{-g}\psi_{n+1} = \epsilon\psi_n, \quad (2)$$

with boundary conditions

$$e^{g}\psi_{N-2} + e^{-g}\psi_0 = \epsilon\psi_{N-1} \quad (3)$$

and

$$e^{g}\psi_{N-1} + V_0\psi_0 + e^{-g}\psi_1 = \epsilon\psi_0. \quad (4)$$

The homogeneous equation can be solved by first solving its characteristic equation

$$\epsilon = \frac{e^{g}}{z} + e^{-g}z. \quad (5)$$

Given an eigenenergy ϵ, there exist two solutions z_1 and z_2 satisfying the constraint condition

$$z_1 z_2 = e^{2g}, \quad (6)$$

and thus the eigenenergies can be represented as $\epsilon = (z_1 + z_2)e^{-g}$. The general wave function takes the form of

$$\psi_n = \alpha_1 z_1^n + \alpha_2 z_2^n, \quad (7)$$

which fulfills the bulk eigenequation of Eq. (2). To obtain the eigensolutions of the whole system, the general ansatz of wave function in Eq. (7) shall also satisfy the boundary conditions. Substituting Eq. (7) into Eqs. (3) and (4) we obtain

$$M_B\begin{pmatrix}\alpha_1\\ \alpha_2\end{pmatrix} = \begin{pmatrix}A(z_1,N) & A(z_2,N)\\ B(z_1,N) & B(z_2,N)\end{pmatrix}\begin{pmatrix}\alpha_1\\ \alpha_2\end{pmatrix} = 0, \quad (8)$$

with

$$A(z,N) = e^{-g}z + e^{g}z^{N-1} - \epsilon + V_0$$

and

$$B(z,N) = e^{g}z^{N-2} + e^{-g} - \epsilon z^{N-1}.$$

The existence of nontrivial solutions for (α_1, α_2) is determined by $\det[M_B] = 0$, which gives rise to the general solution with $\alpha_1 \neq 0, \alpha_2 \neq 0$:

$$\begin{aligned}&\left(z_1^{N+1} - z_2^{N+1}\right) - \frac{t_R}{t_L}\left(z_1^{N-1} - z_2^{N-1}\right)\\ &\quad - \left[1 + \left(\frac{t_R}{t_L}\right)^N\right](z_1 - z_2) - \frac{V_0}{t_L}\left(z_1^N - z_2^N\right)\\ &= 0. \end{aligned} \quad (9)$$

Equations (9) and (6) together determine the solution of z_1 and z_2 exactly. Following the constraint condition of Eq. (6), we can always rewrite the solutions as

$$z_1 = re^{i\theta}, \quad z_2 = re^{-i\theta}, \quad (10)$$

with $r = \sqrt{\frac{t_R}{t_L}} = e^{g}$. Note that θ is not restricted to be real, which is important in determining the properties of the spectrum in latter discussion. Thus Eq. (9) becomes

$$2\cos[N\theta]\sin\theta - (r^{-N} + r^{N})\sin\theta - V_0\sin[N\theta] = 0, \quad (11)$$

or equivalently

$$\frac{\sin\theta[2\cos(N\theta)-2\cosh(Ng)]}{\sin(N\theta)}=V_0. \tag{12}$$

Defining $e^{i\theta}\equiv\beta$, Eq. (11) becomes a polynomial equation of β with an order of $2N$, and hence shall have $2N$ different solutions. However, these solutions come in pairs with θ and $-\theta$, as the equation is invariant with the replacement $\beta\to 1/\beta$. Thus we obtain N independent roots of $\theta=\theta_k$ with $k=1,2,\ldots,N$ labeling the N roots, corresponding to N eigenenergies

$$\epsilon_k=e^{-g}(z_1+z_2)=2\cos\theta_k. \tag{13}$$

We can see that the other N roots $\theta=-\theta_k$ correspond to the same eigenenergies, and the same eigenstates as the coefficients $\alpha_{1,2}$ in Eq. (7) are also exchanged [which can be seen from Eqs. (8) and (10)]. For the PBC case with $V_0=0$, the solutions of Eq. (11) are given by

$$\theta_k=\frac{2k\pi}{N}+ig,\quad k=1,2,\ldots,N.$$

The corresponding eigenenergies are complex and form an ellipse in the complex spectral plane. The eigenstates are given by

$$\psi_n^k=\frac{1}{\sqrt{N}}e^{ng}e^{in\theta_k}=\frac{1}{\sqrt{N}}e^{i2nk\pi/N}, \tag{14}$$

which are uniformly distributed. Note that in this case $A(z_1,N)=0$, allowing us to omit the branch z_2.

We then move on to the more sophisticated case where $V_0\neq 0$. We first rewrite θ_k as $\theta_k=\theta_{k,r}+i\theta_{k,i}$, where $\theta_{k,r}$ and $\theta_{k,i}$ are the real and imaginary part of θ_k. The energy ϵ_k is real either when $\theta_{k,i}=0$ or $\theta_{k,r}=(\pi\pm\pi)/2$, otherwise it acquires a nonzero imaginary amplitude. With further analysis in the Appendix, we find that θ_k is always real when V_0 exceeds a critical value $V_{0,c}$, with

$$V_{0,c}\approx 2\sinh(Ng)\approx e^{Ng}$$

when $N\gg 1$. For relatively small N, the actual critical value $V_{0,c}$ is slightly smaller than $2\sinh(Ng)$. Figure 2(a) shows the imaginary part $\theta_{k,i}$ for the system with $g=1$ and $N=14$ as a function of V_0, with $V_0=2\sinh(Ng)$ given by the gray dotted line. When $0<V_0\lesssim 8.6\times10^4$, we obtain $|\theta_{k,i}|>0$ for every k, and the spectrum still forms an ellipse, as shown in the top panel of Fig. 2(b). We note that the bound state is omitted and the eigenenergies of bulk states are demonstrated in Fig. 2(b). For $8.6\times10^4\gtrsim V_0<2\sinh(Ng)$, $\theta_{k,i}$ becomes zero for some values of k, meaning that a part of the spectrum becomes real, as shown in the middle panel of Fig. 2(b). Due to the pseudo-Hermiticity, the nonreal eigeneneriges in the above two cases always come in pairs with complex conjugated values of θ, and hence the same $|\theta_{k,i}|$. When $V_0\geqslant 2\sinh(Ng)$, all $\theta_{k,i}=0$ for bulk states, i.e., all θ_k and eigenenergies are real, as shown in the bottom panel of Fig. 2(b).

Next we consider the behaviors of the eigenstates. When $V_0>0$, the eigenstates (7) can be written as

$$\psi_n^k=e^{ng}(\alpha_1e^{in\theta_k}+\alpha_2e^{-in\theta_k}).$$

For weak impurity coupling V_0, θ_k are always complex. We can see that the behavior of the wave functions depends not only on θ_k, but also on

$$\begin{aligned}\alpha_1/\alpha_2&=-A(z_2,N)/A(z_1,N)\\&=-\frac{z_2^{N-1}-1/z_2+e^{-g}V_0}{z_1^{N-1}-1/z_1+e^{-g}V_0},\end{aligned} \tag{15}$$

with $z_1=e^{g-\theta_{k,i}+i\theta_{k,r}}$ and $z_2=e^{g+\theta_{k,i}-i\theta_{k,r}}$, obtained by substituting the definition of $A(z,N)$ and Eq. (13). Provided N is sufficiently large, it is straightforward to see that for $g>0$, we shall have $|\alpha_1/\alpha_2|\gg 1$ and $\psi_n^k\propto e^{n(g-\theta_{k,i})}e^{in\theta_{k,r}}$ when $\theta_{k,i}>0$, and $|\alpha_2/\alpha_1|\gg 1$ and $\psi_n^k\propto e^{n(g-|\theta_{k,i}|)}e^{in\theta_{k,r}}$ when $\theta_{k,i}<0$. Similar results can also be obtained for $g<0$. Overall, the wave function can be written as

$$\psi_n^k\approx\alpha e^{\mathrm{sgn}(g)(|g|-|\theta_{k,i}|)n}e^{in\theta_{k,r}}, \tag{16}$$

with $\alpha=\max[\alpha_1,\alpha_2]$, and the wave function decays with increasing n when $|\theta_{k,i}|>|g|$, and with decreasing n when $|\theta_{k,i}|<|g|$. In Fig. 2(a) it is seen that $|\theta_{k,i}|>|g|$ is satisfied only in a regime with small V_0. Therefore we zoom in and provide a clearer view of this regime in Fig. 3(a). When $V_0\lesssim 4.5$, some $\theta_{k,i}$ are seen to be greater than $|g|=1$, and the corresponding eigenstate $|\psi_n|$ decays to the right, as shown in Fig. 3(b1). When $V_0\gtrsim 4.5$, all $\theta_{k,i}$ satisfy $|\theta_{k,i}|<g$, and the corresponding $|\psi_n|$ decays to the left, as shown in Fig. 3(b2).

When $V_0\geqslant 2\sinh(Ng)$, $\theta_{k,i}=0$ is obtained for all bulk states, and the wave function $\psi_n^k\propto e^{gn}e^{in\theta_{k,r}}$ takes the form of skin states. That is, all bulk states now become skin states and all the eigenenergies are real, which is the same situation as the system with $V_0=0$ but under OBC. To see clearly the transition from the nonskin states to skin states, we calculate the averaged inverse participation ratio ⟨IPR⟩ to characterize

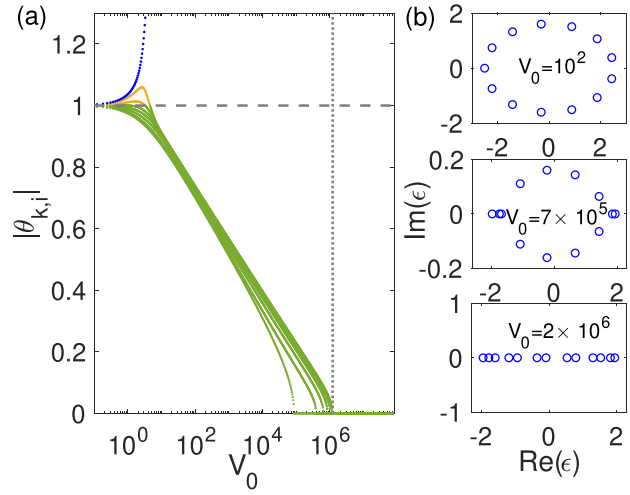

FIG. 2. (a) The absolute value of $\theta_{k,i}=\mathrm{Im}[\theta_k]$ as a function of V_0. Parameters are $g=1$, $N=14$. The blue dots are purely imaginary solutions ($\theta_{k,r}=0$) corresponding to the bound state localized at the impurity ($n=0$). Orange and green dots represent the solutions with $|\theta_{k,i}|>|g|$ and $|\theta_{k,i}|<|g|$, respectively. The rest are the solutions corresponding to the bulk states. The gray dashed line (horizontal) indicates $|\theta_{k,i}|=g=1$. The gray dotted line (vertical) represents $V_0=2\sinh(gN)=1.2\times10^6$ for the chosen parameters. (b) The corresponding complex spectra of bulk states for the system with $V_0=10^2$, 7×10^5, and 2×10^6, respectively.

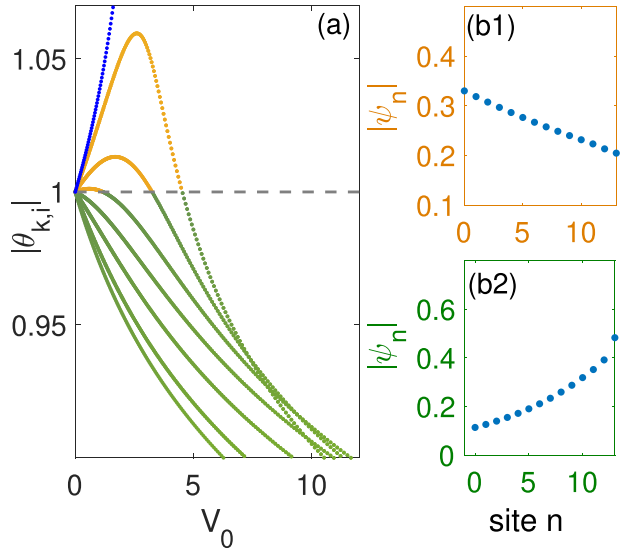

FIG. 3. (a) Zoom in of Fig. 2 at regime of the weak V_0. The gray dashed line indicates $|\theta_{k,i}| = g = 1$. (b) $|\psi_n|$ with different accumulating behaviors for (b1) $|\theta_{k,i}| > |g|$ and (b2) $|\theta_{k,i}| < |g|$.

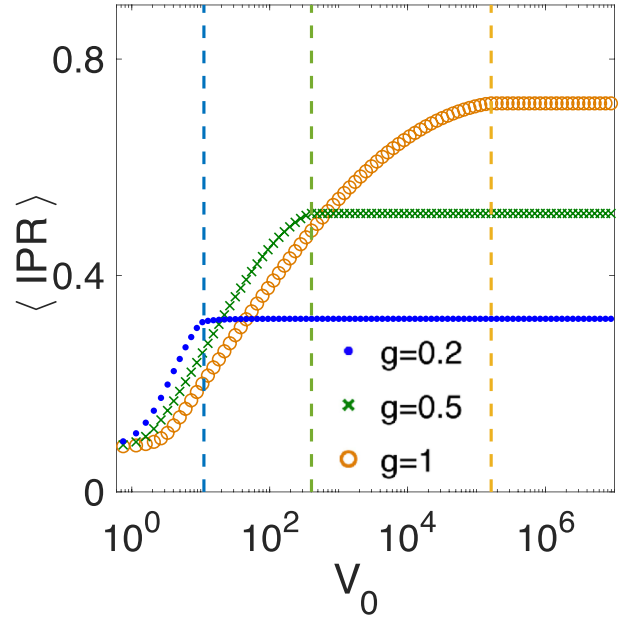

FIG. 4. Average IPR for the system (1) with $N = 14$, $g = 0.2$, 0.5, and 1, respectively. The dashed lines represent the transition points from nonskin to skin states: $V_0 = 2\cosh(Ng)$.

the localization of the system,

$$\langle \mathrm{IPR} \rangle = \frac{1}{N} \sum_k \mathrm{IPR}^{(k)},$$

where $\mathrm{IPR}^{(k)} = \sum_n |\langle n|\psi^k\rangle|^4/(\langle\psi^k|\psi^k\rangle)^2$ and $|\psi^k\rangle$ is the kth right eigenstate of Hamiltonian (1). This quantity is widely used to describe the locality of concerned states, as a fully localized state $\psi_n = \delta_{n_0,n}$ at the position n_0 gives $\mathrm{IPR} = 1$, and a uniformly extended state $\psi_n = e^{i\theta n}/\sqrt{N}$ with real θ corresponds to $\mathrm{IPR} = 1/N$.

The nonskin states given by Eq. (16) are sensitive to V_0 and size N, suggesting that variation of V_0 or N can change $\langle \mathrm{IPR} \rangle$ significantly, analogous to the scale-free accumulating states in Ref. [36]. On the other hand, the locality of skin states only depends on g and shall give a constant $\langle \mathrm{IPR} \rangle$ independent from the impurity strength V_0. We display the $\langle \mathrm{IPR} \rangle$ for all bulk states versus V_0 in Fig. 4, which indicates a clear transition from nonskin to skin states at $V_0 = 2\sinh(Ng)$. That is, as V_0 is increased, $\langle \mathrm{IPR} \rangle$ increases before the transition point of $V_0 = V_{0,c}$, and remains a constant for the skin states after the transition.

III. SINGLE IMPURITY IN THE NONRECIPROCAL SSH MODEL

Next we extend our study to the nonreciprocal SSH model [51] with a single impurity under PBC, as displayed in Fig. 1(b), which can also be exactly solved. Unlike the single-band HN model, the nonreciprocal SSH model exhibits nontrivial band topology with different topological transition points (gap closing points) under PBC and OBC, making the impurity problem more intriguing as the impurity effectively changes the boundary conditions. The Hamiltonian of this model is given by

$$H_{\mathrm{SSH}} = \sum_{n=0}^{N-1} [t(e^{-g}|n,A\rangle\langle n,B| + e^{g}|n,B\rangle\langle n,A|) + t'(|n,B\rangle\langle n+1,A| + \mathrm{H.c.})] + V_0|0,A\rangle\langle 0,A|, \quad (17)$$

with A and B indexes for different sublattices, $|N, A(B)\rangle \equiv |0, A(B)\rangle$, N is the total number of unit cells, V_0 is the impurity strength, and t' ($te^{\pm g}$) is the intercell (right and left intracell) hopping term(s). The energy unit is set to be $t = 1$ for latter convenience.

When $V_0 = 0$, through the Fourier transformation, the Hamiltonian of the nonreciprocal SSH model without the impurity can be represented as

$$H_0(k) = h_x\sigma_x + h_y\sigma_y$$

in the momentum space, where $h_x = t'\cos k + \cosh g$, $h_y = t'\sin k - i\sinh g$ with $0 \leqslant k < 2\pi$, and $\sigma_{x,y}$ are the Pauli matrices. The eigenenergies are given by

$$E = \pm\sqrt{(h_x + ih_y)(h_x - ih_y)} = \pm\sqrt{(t'e^{ik} + e^{g})(t'e^{-ik} + e^{-g})}.$$

The two-band structure of this model allows line-gap topology to emerge in this system, and the phase boundaries can be determined by the gap closing conditions of the system [2,3],

$$t' = -e^{\pm g} \quad \text{and} \quad t' = e^{\pm g}. \quad (18)$$

Note that through the similarity transformation, the model (17) with $V_0 = 0$ under OBC becomes the Hermitian SSH model, where the topological transition points (gap-closing points) are given by $t' = \pm t = \pm 1$. In other words, the spectra of systems under PBC and OBC have different gap-closing points [2,6,37], allowing us to identify the different PBC- and

OBC-like behaviors of the system under different impurity strengths, as discussed later.

When $V_0 \neq 0$, we can solve Eq. (17) by taking the wave function as $|\psi\rangle = \sum_n (\psi_{A,n}|n, A\rangle + \psi_{B,n}|n, B\rangle)$. The stationary Schrödinger equation $H_{\rm SSH}|\psi\rangle = E|\psi\rangle$ is equivalent to the following difference equations:

$$e^g \psi_{A,n-1} + t' \psi_{A,n} = E \psi_{B,n-1}, \tag{19}$$

$$t' \psi_{B,n-1} + e^{-g} \psi_{B,n} + \delta_{n,0} V_0 \psi_{A,n} = E \psi_{A,n}, \tag{20}$$

where E is the eigenenergy. Equation (19) gives us

$$\psi_{B,n} = \frac{e^g}{E} \psi_{A,n} + \frac{t'}{E} \psi_{A,n+1}. \tag{21}$$

We can decouple ψ_A and ψ_B by substituting Eq. (21) into Eq. (20), which yields

$$e^g \psi_{A,n-1} + e^{-g} \psi_{A,n+1} + \delta_{n,0} \frac{E V_0}{t'} \psi_{A,n} = \frac{E^2 - t'^2 - 1}{t'} \psi_{A,n}. \tag{22}$$

It is obvious that Eq. (22) under the following substitution:

$$V_0 \to \frac{E V_0}{t'}, \tag{23}$$

$$\epsilon \to \frac{E^2 - t'^2 - 1}{t'}, \tag{24}$$

is identical to Eq. (2) with boundary conditions (3) and (4). Thus to solve Eq. (22), we can directly use the results of the impurity problem in the HN model in Sec. II. That is, by substituting Eqs. (24) and (23) into Eqs. (13) and (12), we obtain

$$E = \pm \sqrt{1 + t'^2 + 2t' \cos\theta}$$

and

$$\frac{t' \sin(\theta)[2\cos(N\theta) - 2\cosh(Ng)]}{\pm \sqrt{1 + t'^2 + 2t' \cos\theta}\, \sin(N\theta)} = V_0, \tag{25}$$

respectively. Following our analysis of Eq. (12), the transition point from nonskin states to skin states can be determined by

$$V_{0,c} = 2t^* \sinh(Ng) \approx t^* e^{Ng},$$

with $t^* = \min\{1, t'\}$ for large N or g. $V_{0,c}$ increases exponentially with the lattice size N. At small V_0 far from the critical value, all θ_k for bulk states are complex. The spectra are similar to the PBC system with $V_0 = 0$. The topological phase transition occurs at $t' = \pm e^{\pm g}$, as shown in Fig. 5(a). When $V_0 \geqslant 2t^* \sinh(Ng)$, all θ_k for bulk states are real. So all the bulk states become the skin states and all the eigenenergies are real, analogous to the system with $V_0 = 0$ under OBC. The topological phase transition then takes place at $t' = \pm 1$, as shown in Fig. 5(b).

Finally, we display $\langle \text{IPR} \rangle$ of all bulk states versus V_0 in Fig. 6 with $t' = 0.5$ and $t' = 2$, respectively. Figure 6 demonstrates a clear transition from nonskin states to skin states at $V_0 = \sinh(Ng)$ with $t' = 0.5$ and $V_0 = 2\sinh(Ng)$ with $t' = 2$ for $N = 14$. $\langle \text{IPR} \rangle$ increase for the nonskin states with increasing V_0, and remains constant for the skin states.

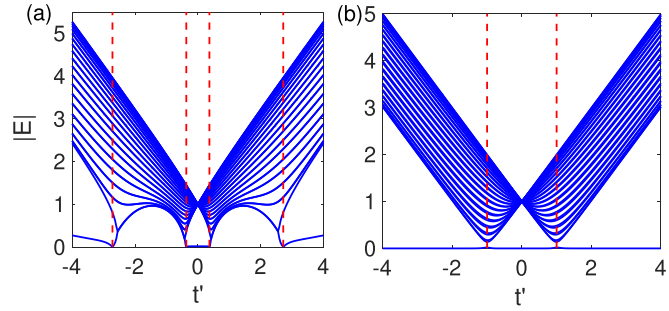

FIG. 5. Spectrum $|E|$ for the system (17) with $N = 20$, $g = 1$, (a) $V = 2\cosh(4)$ and (b) $V = 2\cosh(N + 1)$, respectively. The dashed lines in (a) represent the gap-closing points $t' = \pm e^{\pm g}$. The dashed lines in (b) represent the gap-closing points $t' = \pm 1$.

IV. QUANTIZED RESPONSE OF THE SPECTRAL TOPOLOGY IN THE IMPURITY MODELS

In previous sections we have exactly solved the single-impurity problem for the HN model and SSH model, both exhibit the NHSE and thus possess a nontrivial spectral topology [28–30]. It has recently been discovered that a quantized response corresponding to the spectral topology can be extracted from the system's Green's function element, in the process of tuning the boundary condition from PBC to OBC continuously [39]. Therefore we expect a similar phenomenon to arise also in our model, as a strong impurity strength effectively acts as the OBC.

Following Ref. [39] we define quantities as

$$\nu_{0(N-1)} = \frac{\partial \ln G_{0(N-1)}}{\partial \ln V_0}, \quad \nu^B_{0(N-1)} = \frac{\partial \ln G^B_{0(N-1)}}{\partial \ln V_0} \tag{26}$$

for the HN model and the SSH model, respectively, with

$$G_{0(N-1)} = \langle 0 | G_{\rm HN} | N - 1 \rangle$$

and

$$G^B_{0(N-1)} = \langle 0, B | G_{\rm SSH} | N - 1, B \rangle$$

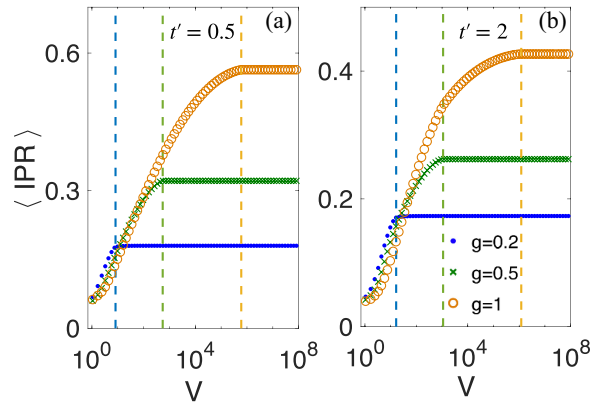

FIG. 6. (a) Average IPR for the system (17) with $N = 14$, $t' = 0.5$, $g = 0.2$, 0.5, and 1, respectively. The dashed lines represent the transition points from nonskin to skin states, $V_{0,c} = \sinh(Ng)$. (b) Average IPR for the system (17) with $N = 14$, $t' = 2$, $g = 0.2$, 0.5, and 1, respectively. The dashed lines represent the transition points from nonskin to skin states, $V_{0,c} = 2\sinh(Ng)$.

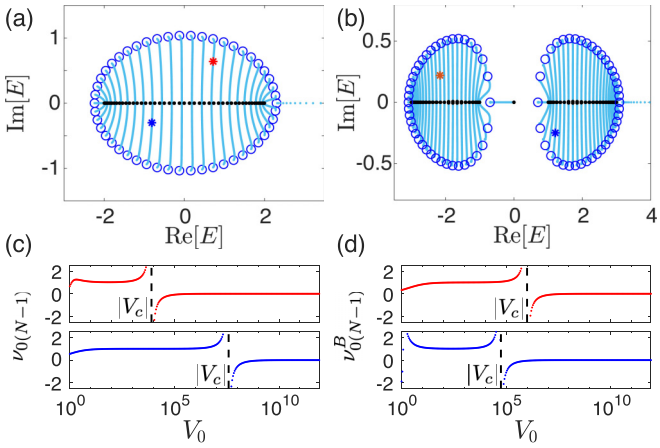

FIG. 7. (a) and (b) The spectra with $V_0 = 0$ (blue circles) and $V_0 = 10^{12}$ (black dots) for the HN model and the SSH model, respectively. Cyan dotted,curves illustrate the spectra with V_0 varying from 0 to 10^{12}, namely the spectral flow from PBC to strong impurity limit, the latter effectively gives the OBC. Red and blue stars are the chosen reference energies E_r for calculating $\nu_{0(N-1)}$ and $\nu^B_{0(N-1)}$, $E_r = 0.72 + 0.64i$ (red) and $-0.81 - 0.3i$ (blue) in (a), and $E_r = -2.16 + 0.22i$ (red) and $1.21 - 0.25i$ in (b). (c) and (d) The defined quantities $\nu_{0(N-1)}$ and $\nu^B_{0(N-1)}$ versus V_0 for different E_r, indicated by the stars with the same colors in (a) and (b). The black dash lines indicate the critical value $|V_c|$ obtained from Eqs. (12) and (25) by requiring $\epsilon = E_r$. Note that the obtained V_c takes complex values as E_r does not exactly fall on the spectral flow.

the off-diagonal elements of the Green's functions $G_{\rm HN}$ of the HN model and $G_{\rm SSH}$ of the SSH model,

$$G_{\rm HN} = (E_r - H_{\rm HN})^{-1}, \quad G_{\rm SSH} = (E_r - H_{\rm SSH})^{-1}. \quad (27)$$

E_r is a chosen complex reference energy to define the spectral winding [29,30,39]. In our models, the spectral winding number is $\nu = 1$ for E_r enclosed by the PBC spectra in the complex plane. In such cases, $\nu_{0(N-1)}$ and $\nu^B_{0(N-1)}$ are expected to jump from 1 to 0 for the concerned models when V_0 is increased and reaches a critical value, where the spectra coincide with E_r [39].

In Fig. 7 we illustrate the defined quantities as functions of V_0 for several different E_r enclosed by the PBC spectrum at $V_0 = 0$. It is seen that each of $\nu_{0(N-1)}$ and $\nu^B_{0(N-1)}$ roughly exhibits a plateau at 1, and jumps to 0 after a critical value $V_0 = V_c$. Note that V_c is distinguished from $V_{0,c}$ in previous sections, which describes the transition to a fully real spectrum. The spectrum forms a shrinking ellipse with increasing V_0, passing through E_r at $V_0 = V_c$, after which the spectral winding jumps from 1 to 0. Therefore, for a given E_r, we can require it to be an eigenenergy ϵ of the system, then determine V_c through Eqs. (12) and (25) for the two models, respectively.

We would also like to point out that in a finite-size system, the spectral flow [cyan dotted curves in Figs. 7(a) and 7(b)] from $V_0 = 0$ to $V_0 \to \infty$ cannot cover the regime enclosed by the PBC ellipse spectrum completely. Strictly speaking, a real V_c can be obtained only when E_r exactly falls along the spectral flow. Nevertheless, numerically we can choose E_r close enough to the spectral flow [e.g., blue and red stars in Figs. 7(a) and 7(b)], and the absolute value of the obtained V_c are seen to be in good consistency with the jump of $\nu_{0(N-1)}$ and $\nu^B_{0(N-1)}$ in Figs. 7(c) and 7(d), respectively. It is also seen from the figures that $\nu_{0(N-1)}$ and $\nu^B_{0(N-1)}$ deviate from the quantized value when V_0 is small. On the other hand, the critical value V_c of the impurity shall also decrease with N, in analog to the hopping impurity studied in Ref. [39]. Therefore the first plateau may not be clearly seen for a smaller system, where $\nu_{0(N-1)}$ or $\nu^B_{0(N-1)}$ may jump to the next plateau before it reaches its quantized value and becomes flat.

V. SUMMARY

In summary, we have exactly solved the impurity problem in the HN model and the SSH model. The exact solutions of finite-size systems reveal a transition for the bulk states from nonskin states to skin states when increasing the impurity strength V_0, and the corresponding complex eigenenergies also become real after the transition. The critical value $V_{0,c}$ of the impurity for the transition depends on both the lattice size N and the parameter g describing the nonreciprocity, and increases as $V_{0,c} \approx \sinh Ng$. Such a transition indicates that a strong impurity acts as an open boundary for the NHSE in nonreciprocal non-Hermitian systems, as the impurity suppresses the hoppings between it and its neighbor sites. Different bulk states are also found to reach the OBC limit at different critical values of $V_{0,c}$. We have also extended our study to the single-impurity problem of the SSH model, which can be mapped to the HN model, and exact solutions can be obtained accordingly. Our exact solutions are also proven useful for investigating the spectral topological transition in the concerned models. In more complicated cases with longer-range hoppings, a single impurity can be bypassed by the longer-range hoppings which directly connect lattice sites on the two sides of the impurity. In other words, a single impurity may not be able to induce an OBC limit to systems with longer range hoppings, and such a scenario is yet to be explored.

Note added in proof. In preparation of our manuscript, we become aware of a related work [52], in which the OBC skin eigenstates are obtained using the Green's function method by placing an infinite impurity on a single lattice site.

ACKNOWLEDGMENTS

The work is supported by NSFC under Grant No. 11974413 and the National Key Research and Development Program of China (2016YFA0300600 and 2016YFA0302104). L.L. acknowledges funding support by the Guangdong Basic and Applied Basic Research Foundation (No. 2020A1515110773).

APPENDIX: THE TRANSITION POINT BETWEEN COMPLEX AND REAL SPECTRA

From Fig. 2 we see that the spectrum of the HN model with an impurity becomes purely real when V_0 is large enough. To identify the critical value $V_{0,c}$ for this transition, we rewrite Eq. (11) as

$$f_1(\theta) = f_2(\theta), \quad (A1)$$

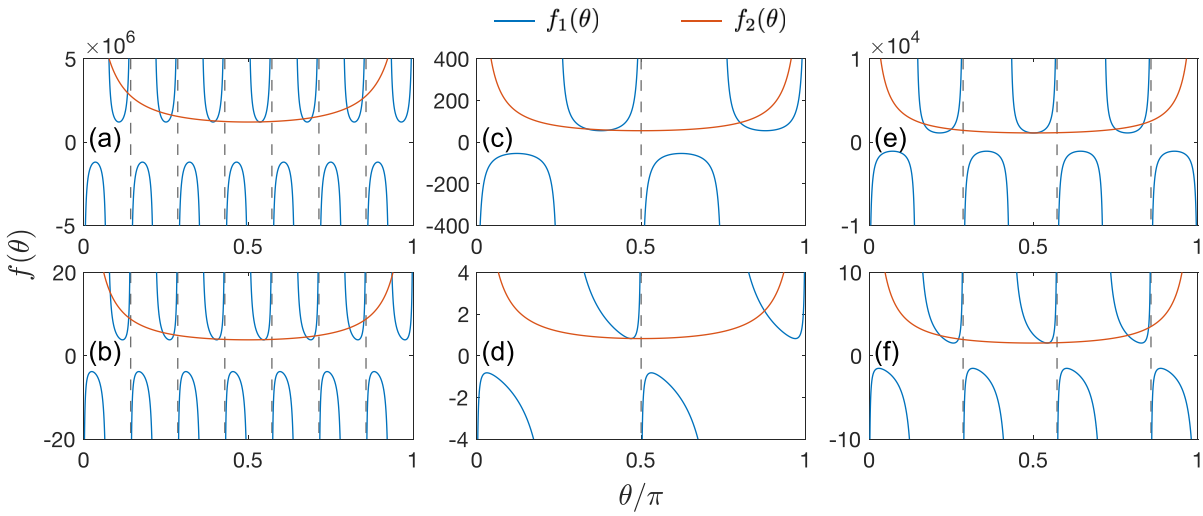

FIG. 8. $f_1(\theta)$ and $f_2(\theta)$ with $V_0 = 2\sinh[Ng]$ as a function of θ. Parameters given in (a) $N = 14$, $g = 1$; (b) $N = 14$, $g = 0.1$; (c) $N = 4$, $g = 1$; (d) $N = 4$, $g = 0.1$; (e) $N = 7$, $g = 1$; and (f) $N = 7$, $g = 0.1$. Dashed lines separate different period of $f_1(\theta)$.

where

$$f_1(\theta) = \frac{2\cos[N\theta] - (r^{-N} + r^N)}{\sin[N\theta]} = \frac{2\cos[N\theta] - 2\cosh(Ng)}{\sin[N\theta]} \tag{A2}$$

and

$$f_2(\theta) = \frac{V_0}{\sin\theta}. \tag{A3}$$

Note that the energy

$$\epsilon = 2\cos\theta$$

is real with either purely real or imaginary θ. We shall first focus on the case with real θ, which has a period of 2π. On the other hand, θ and $-\theta$ correspond to the same eigensolution of the system, as discussed in the main text. Therefore we only need to focus on the behavior of $f_{1,2}(\theta)$ with $\theta \in (0, \pi)$. Here the two points of $\theta = 0$ and π are excluded, because at such values we shall obtain a nonphysical solution with a vanishing wave function $\phi_n = 0$ by substituting Eq. (10) into Eq. (8) in the main text. If $f_1(\theta)$ and $f_2(\theta)$ have $N - x$ intersection points, Eq. (A1) has $N - x$ real and x complex solutions, where $0 \leqslant x \leqslant N$. In this regime, $f_2(\theta)$ is a positive definite function, which is symmetrical of $\theta = \pi/2$ and its minimum value is given by $f_{2,\min} = f_2(\pi/2) = V_0$. $f_1(\theta)$ has a period of $2\pi/N$ (separated by the dash lines in Fig. 8), and satisfies $f_1(\theta) > 0$ in the regimes of

$$\theta \in \left(\frac{(2n+1)\pi}{N}, \frac{(2n+2)\pi}{N}\right), \quad n = 0, 1, \ldots, \left\lfloor \frac{N}{2} \right\rfloor - 1, \tag{A4}$$

i.e., the right half of each period. In each interval, $f_1(\theta)$ decreases monotonically at first and meets its minimum value $f_{1,\min} = 2\sinh Ng$ at

$$\theta = \frac{1}{N}\left(-\arccos\frac{1}{\cosh(Ng)} + 2n\pi\right), \quad n = 1, \ldots, [N/2],$$

and increases monotonically again (see Fig. 8). Therefore, $f_1(\theta)$ and $f_2(\theta)$ generally intersect twice within each of the $\lfloor N/2 \rfloor$ intervals given by Eq. (A4). However, for an even N, the second intersection in the last interval tends to $\theta = \pi$ where both $f_1(\theta)$ and $f_2(\theta)$ tend to infinity. Thus we obtain $N - 1$ intersections of $f_1(\theta)$ and $f_2(\theta)$ in total for $\theta \in (0, \pi)$, with either an even [Figs. 8(a)–8(d)] or an odd N [Figs. 8(e) and 8(f)]. When $N \to \infty$, the period of $f_1(\theta)$ approaches zero, meaning we can find the minimum value of $f_1(\theta)$ infinitely close to $\pi/2$, leading to

$$\lim_{N\to\infty} V_{0,c} = 2\sinh(Ng),$$

and two intersections around this nadir emerge when $V_{0,c} > 2\sinh(Ng)$. As we can infer from Figs. 8(c) and 8(d), $2\sinh(Ng)$ makes a good approximation of $V_{0,c}$ also for small N. The exact critical value of $V_{0,c}$ can only be smaller than $2\sinh(Ng)$, as $f_2(\theta)$ gets larger when θ diverges away from $\pi/2$, and hence approaches the minimums of $f_1(\theta)$ at a smaller V_0. To conclude, when $V_0 \geqslant 2\sinh(Ng)$, $f_2(\theta)$ and $f_1(\theta)$ shall have $N - 1$ intersections for $\theta \in (0, \pi)$, corresponding to $N - 1$ real solutions of the bulk states.

For imaginary θ, $f_1(\theta)$ and $f_2(\theta)$ are mostly monotonic and only gives a single intersection for $\mathrm{Im}[\theta] \in (0, \infty)$, regardless of the value of N and g, corresponding to the bound state.

[1] N. J. Higham and L. N. Trefethen, *Spectra and Pseudospectra: The Behavior of Nonnormal Matrices and Operators* (Princeton University Press, Princeton, NJ, 2005).

[2] S. Yao and Z. Wang, Edge States and Topological Invariants of Non-Hermitian Systems, Phys. Rev. Lett. **121**, 086803 (2018).

[3] C. Yin, H. Jiang, L. Li, R. Lü, and S. Chen, Geometrical meaning of winding number and its characterization of topological

phases in one-dimensional chiral non-Hermitian systems, Phys. Rev. A **97**, 052115 (2018).
[4] Z. Gong, Y. Ashida, K. Kawabata, K. Takasan, S. Higashikawa, and M. Ueda, Topological Phases of Non-Hermitian Systems, Phys. Rev. X **8**, 031079 (2018).
[5] V. M. Martinez Alvarez, J. E. Barrios Vargas, and L. E. F. Foa Torres, Non-Hermitian robust edge states in one dimension: Anomalous localization and eigenspace condensation at exceptional points, Phys. Rev. B **97**, 121401(R) (2018).
[6] F. K. Kunst, E. Edvardsson, J. C. Budich, and E. J. Bergholtz, Biorthogonal Bulk-Boundary Correspondence in Non-Hermitian Systems, Phys. Rev. Lett. **121**, 026808 (2018).
[7] S. Yao, F. Song, and Z. Wang, Non-Hermitian Chern Bands, Phys. Rev. Lett. **121**, 136802 (2018).
[8] L. Jin and Z. Song, Bulk-boundary correspondence in non-Hermitian systems, Phys. Rev. B **99**, 081103(R) (2019).
[9] C. H. Lee and R. Thomale, Anatomy of skin modes and topology in non-Hermitian systems, Phys. Rev. B **99**, 201103(R) (2019).
[10] K. Kawabata, K. Shiozaki, and M. Ueda, Anomalous helical edge states in a non-Hermitian Chern insulator, Phys. Rev. B **98**, 165148 (2018).
[11] C. H. Lee, L. Li, and J. Gong, Hybrid Higher-Order Skin-Topological Modes in Non-Reciprocal Systems, Phys. Rev. Lett. **123**, 016805 (2019).
[12] L. Herviou, J. H. Bardarson, and N. Regnault, Defining a bulk-edge correspondence for non-Hermitian Hamiltonians via singular-value decomposition, Phys. Rev. A **99**, 052118 (2019).
[13] W. B. Rui, Y. X. Zhao, and A. P. Schnyder, Classification of massive Dirac models with generic non-Hermitian perturbations, Phys. Rev. B **99**, 241110(R) (2019).
[14] F. Song, S. Yao, and Z. Wang, Non-Hermitian Topological Invariants in Real Space, Phys. Rev. Lett. **123**, 246801 (2019).
[15] S. Longhi, Probing non-Hermitian skin effect and non-Bloch phase transitions, Phys. Rev. Research **1**, 023013 (2019).
[16] H. Jiang, R. Lu, and S. Chen, Topological invariants, zero mode edge states and finite size effect for a generalized non-reciprocal Su-Schrieffer-Heeger model, Eur. Phys. J. B **93**, 125 (2020).
[17] Z. Ozcakmakli Turker and C. Yuce, Open and closed boundaries in non-Hermitian topological systems, Phys. Rev. A **99**, 022127 (2019).
[18] L. Xiao, T. Deng, K. Wang, G. Zhu, Z. Wang, W. Yi, and P. Xue, Non-Hermitian bulk-boundary correspondence in quantum dynamics, Nat. Phys. **16**, 761 (2020).
[19] X. R. Wang, C. X. Guo, and S. P. Kou, Defective edge states and anomalous bulk-boundary correspondence in non-Hermitian topological systems, Phys. Rev. B **101**, 121116(R) (2020).
[20] H. Shen, B. Zhen, and L. Fu, Topological Band Theory for Non-Hermitian Hamiltonians, Phys. Rev. Lett. **120**, 146402 (2018).
[21] K. Yokomizo and S. Murakami, Non-Bloch Band Theory of Non-Hermitian Systems, Phys. Rev. Lett. **123**, 066404 (2019).
[22] Y. Ashida, Z. Gong, and M. Ueda, Non-Hermitian physics, Adv. Phys. **69**, 3 (2020).
[23] F. K. Kunst and V. Dwivedi, Non-Hermitian systems and topology: A transfer-matrix perspective, Phys. Rev. B **99**, 245116 (2019).
[24] R. Chen, C.-Z. Chen, B. Zhou, and D.-H. Xu, Finite-size effects in non-Hermitian topological systems, Phys. Rev. B **99**, 155431 (2019).
[25] J. C. Budich and E. J. Bergholtz, Non-Hermitian Topological Sensors, Phys. Rev. Lett. **125**, 180403 (2020).
[26] K. Kawabata, N. Okuma, and M. Sato, Non-Bloch band theory of non-Hermitian Hamiltonians in the symplectic class, Phys. Rev. B **101**, 195147 (2020).
[27] R. Koch and J. C. Budich, Bulk-boundary correspondence in non-Hermitian systems: Stability analysis for generalized boundary conditions, Eur. Phys. J. D **74**, 70 (2020).
[28] D. S. Borgnia, A. J. Kruchkov, and R.-J. Slager, Non-Hermitian Boundary Modes and Topology, Phys. Rev. Lett. **124**, 056802 (2020).
[29] K. Zhang, Z. Yang, and C. Fang, Correspondence between Winding Numbers and Skin Modes in Non-Hermitian Systems, Phys. Rev. Lett. **125**, 126402 (2020).
[30] N. Okuma, K. Kawabata, K. Shiozaki, and M. Sato, Topological Origin of Non-Hermitian Skin Effects, Phys. Rev. Lett. **124**, 086801 (2020).
[31] L. Li, C. H. Lee, S. Mu, and J. Gong, Critical non-Hermitian skin effect, Nat. Commun. **11**, 5491 (2020).
[32] C.-H. Liu, K. Zhang, Z. Yang, and S. Chen, Helical damping and dynamical critical skin effect in open quantum systems, Phys. Rev. Research **2**, 043167 (2020).
[33] W.-T. Xue, M.-R. Li, Y.-M. Hu, F. Song, and Z. Wang, Simple formulas of directional amplification from non-Bloch band theory, Phys. Rev. B **103**, L241408 (2021).
[34] C. C. Wanjura, M. Brunelli, and A. Nunnenkamp, Topological framework for directional amplification in driven-dissipative cavity arrays, Nat. Commun. **11**, 3149 (2020).
[35] Y. Xiong, Why does bulk boundary correspondence fail in some non-Hermitian topological models, J. Phys. Commun. **2**, 035043 (2018).
[36] L. Li, C. H. Lee, and J. Gong, Impurity induced scale-free localization, Commun Phys **4**, 42 (2021).
[37] C.-X. Guo, C.-H. Liu, X.-M. Zhao, Y. Liu, and S. Chen, Exact solution of non-Hermitian systems with generalized boundary conditions: Size-dependent boundary effect and fragility of skin effect, arXiv:2102.03781.
[38] C. H. Lee, L. Li, R. Thomale, and J. Gong, Unraveling non-Hermitian pumping: Emergent spectral singularities and anomalous responses, Phys. Rev. B **102**, 085151 (2020).
[39] L. Li, S. Mu, C. H. Lee, and J. Gong, Quantized classical response from spectral winding topology, arXiv:2012.08799.
[40] J. C. Y. Teo and C. L. Kane, Topological defects and gapless modes in insulators and superconductors, Phys. Rev. B **82**, 115120 (2010).
[41] J. Lu, W.-Y. Shan, H.-Z. Lu, and S.-Q. Shen, Non-magnetic impurities and in-gap bound states in topological insulators, New J. Phys. **13**, 103016 (2011).
[42] L.-J. Lang and S. Chen, Topologically protected mid-gap states induced by impurity in one-dimensional superlattices, J. Phys. B: At. Mol. Opt. Phys. **47**, 065302 (2014).
[43] R.-J. Slager, L. Rademaker, J. Zaanen, and L. Balents, Impurity-bound states and Green's function zeros as local signatures of topology, Phys. Rev. B **92**, 085126 (2015).

[44] L. Kimme and T. Hyart, Existence of zero-energy impurity states in different classes of topological insulators and superconductors and their relation to topological phase transitions, Phys. Rev. B **93**, 035134 (2016).

[45] C. Liu, and S. Chen, Topological classification of defects in non-Hermitian systems, Phys. Rev. B **100**, 144106 (2019).

[46] Y. Liu and S. Chen, Diagnosis of bulk phase diagram of non-reciprocal topological lattices by impurity modes, Phys. Rev. B **102**, 125103 (2020).

[47] X.-Q. Sun, P.-H. Zhu, and T. L. Hughes, Geometric response and disclination-induced skin effects in non-Hermitian systems, arXiv:2102.05667.

[48] A. Panigrahi, R. Moessner, and B. Roy, Non-Hermitian dislocation modes: Stability and melting across exceptional points, arXiv:2105.05244.

[49] F. Schindler and A. Prem, Dislocation skin effect in non-Hermitian crystals, arXiv:2106.00039.

[50] N. Hatano and D. R. Nelson, Localization Transitions in Non-Hermitian Quantum Mechanics, Phys. Rev. Lett. **77**, 570 (1996).

[51] W. P. Su, J. R. Schrieffer, and A. J. Heeger, Solitons in Polyacetylene, Phys. Rev. Lett. **42**, 1698 (1979).

[52] F. Roccati, Non-Hermitian skin effect as an impurity problem, arXiv:2105.01197.